Available online at www.sciencedirect.com
ScienceDirect
International Journal of Heat and Mass Transfer 51 (2008) 2914–2924
International Journal of HEAT and MASS TRANSFER
www.elsevier.com/locate/ijhmt

Effects of miter bend on pressure drop and flow structure in micro-fluidic channels

Renqiang Xiong, Jacob N. Chung *

Department of Mechanical and Aerospace Engineering, University of Florida, Gainesville, FL 32611-6300, USA

Received 21 May 2007; received in revised form 10 September 2007
Available online 20 February 2008

Abstract

The characteristics of a pressure-driven water flow including flow micro-structures and pressure drops are investigated in serpentine micro-channels with miter bends. The micro-channels have rectangular cross-sections with hydraulic diameters of 0.209 mm, 0.412 mm and 0.622 mm, respectively. To segregate the bends and entrance effects individually from the total pressure drop, for each size three types of micro-channels: straight short, straight long and long serpentine, were fabricated to get the reliable pressure data without entrance effect. A micron-resolution particle image velocimetry system (micro-PIV) was develop and used to obtain the detailed velocity vector field. The experimental results show that the vortices around the outer and inner walls of the bend do not form when $Re < 100$. Those vortices appear and continue to develop with increasing Re number when Re is larger than a value around 100, and the shape and size of the vortices almost remain constant when the Re is larger than a value around 1000. The experimentally observed additional pressure drop due to the bend is commensurate with the strength of the calculated vortices. The bend loss coefficient K_b was observed to be related only with the Re number when $Re < 100$, but with the Re number and channel size when $Re > 100$. It almost keeps constant and changes in the range of $\pm 10\%$ when the Re is larger than a threshold value somewhere in 1000–1500.

Keywords: Miter bend; Micro-PIV; Entrance flow; Pressure drop

1. Introduction

In recent years, the proliferation of MEMS and micro-fluidic devices has resulted in the use of micro-channels in many applications including propulsion and power generation of micro-air vehicles, micro-scaled cooling systems of electronic devices, micro-satellites, etc. [1]. Because of the wide range of uses for micro-channels, it is important to be able to well predict their behavior which requires a good knowledge of flow characteristics in straight and serpentine micro-channels [2–6].

Flow characteristics in circular and non-circular macro-ducts with curved bends have been extensively studied [7,8]. However, there were limited literatures on flow characteristics in the channels with miter bends [9–13]. Though the flow in macro-systems with bends had gained many achievements, research on flow characteristics in micro-systems with bends just started. Recently Lee et al. [14] researched on the gas flow in micro-channels having the dimensions $20 \times 1 \times 5810\ \mu m^3$ with bends of miter, curved and double-turn design. They found the flow rate through the channel with the miter bend was the lowest at a certain inlet pressure and the largest drop was found in the miter bend with the lowest flow rate, and the secondary flow could develop in micro-channels, contrary to expectations. Maharudrayya et al. [15] studied the pressure losses and flow structures of laminar flow through serpentine channels with miter bends by a CFD code but they did not consider the micro-scale effect.

To evaluate the bend loss coefficient, the bend additional pressure drop must be obtained. It can be measured by subtracting the frictional pressure drop of a straight micro-channel from the total serpentine micro-channel pressure

* Corresponding author. Tel.: +1 352 392 9067; fax: +1 352 392 1071.
E-mail address: jnchung@ufl.edu (J.N. Chung).

0017-9310/$ - see front matter © 2007 Published by Elsevier Ltd.
doi:10.1016/j.ijheatmasstransfer.2007.09.018

Nomenclature

A	area (m^2)
B	coefficient in Eq. (8)
dP/dX	pressure gradient (Pa/m)
D	diameter (mm)
f	fraction factor
f_{app}	apparent friction factor
K	pressure drop defect
K_b	bend loss coefficient
L	length of micro-channels (mm)
L_d	entrance length (mm)
n	refraction index
N	number of miter bends
NA	numerical aperature
P	pressure (Pa)
Q	flow rate (ml/min)
Re	Reynolds number
S	depth of micro-channels (mm)
u	local velocity at x-direction (m/s)
U	mean velocity (m/s)
W	width of micro-channels (mm)
x	the coordinate along the length
x^+	dimensionless entrance length
y	the coordinate along the width
Z_m	measurement depth (μm)

Greek symbols

Δ	variable difference
α	aspect ratio
Γ	circulation (mm^2/s)
λ	wavelength of light in a vacuum (μm)
μ	viscosity (kg/m s)
θ	light collection angle
ρ	density (kg/m^3)

Subscripts

b	90° bend
c	cross-section
dev	developing and developed flow
exp	experimental result
fd	fully developed
h	hydraulic diameter
io	inlet and outlet
l	long straight micro-channel
p	fluorescent particles
S	serpentine micro-channel
sh	short straight micro-channel

drop. For the past 15 years, many scientists have published numerous papers on the relationship between the friction factor and Re number in straight micro-channels. Some of them found for a liquid flow an increase of the friction factor with the Re number including Wu and Little [16], Peng and Peterson [17], Mala and Li [18], Qu et al. [19], and Li et al. [20]. They attributed it to surface roughness effect or the early transition to turbulent flow ($Re = 300$–500) in straight micro-channels. However, recent studies showed general agreement with theoretical macro-scale predictions for friction factors including Judy et al. [21], Wu and Cheng [22], Hetsroni et al. [23], Kohl et al. [24], Hwang and Kim [25]. They attributed the deviation from the theoretical prediction in the previous literatures to the size and measurement uncertainties or not count the entrance effect [26]. Some review articles can also be found in Koo and Kleinstreuer [27], Bayraktar and Pidugu [28], and Hassan [29]. To secure reliable data for the straight micro-channels, experiments for the frictional pressure drop were also done here.

In this work, three groups of micro-channels were fabricated and used. Each group has three micro-channels with the same channel size: straight long, straight short and single serpentine with miter bends. The straight long and straight short micro-channels were used to achieve the reliable frictional pressure drop in straight micro-channels without inlet and outlet losses, and the serpentine micro-channels were used to obtain the bend additional pressure drop. The main objective of this study is to achieve (1) the bend additional pressure drop and bend loss coefficient for serpentine micro-channels, and (2) the flow micro-structures under different Re numbers in serpentine micro-channels by using a micro-PIV system.

2. Experimental apparatus

Fig. 1 shows the photographs of three groups of the micro-channels, schematics of the straight micro-channel and the inlet/outlet. The micro-channels were etched in a silicon substrate and then a Pyrex thin cover glass plate was anodically bonded on the top of the substrate. Two small connection tubes which can be inserted into the inlet and outlet assembly were connected with the small reservoirs. Each of the serpentine micro-channels has five straight channels with the same size and eight miter bends as shown in Fig. 1(a). The inlet and outlet assemblies which contain tubing diameter change, tees and elbows are illustrated in Fig. 1(c). Table 1 listed the dimensions of three groups of micro-channels.

Fig. 2 shows the schematic of the experimental apparatus used to investigate the pressure-driven water flow in micro-channels. It includes two Nd:YAG lasers (Continuum), a timing controller (Labsmith), a CCD camera (Cooke), a filter cube (Olympus), a 0.5× magnification lens (Olympus), a microscope (Olympus), some optical lenses (Edmund), a syringe infusion pump (Cole-Parmer

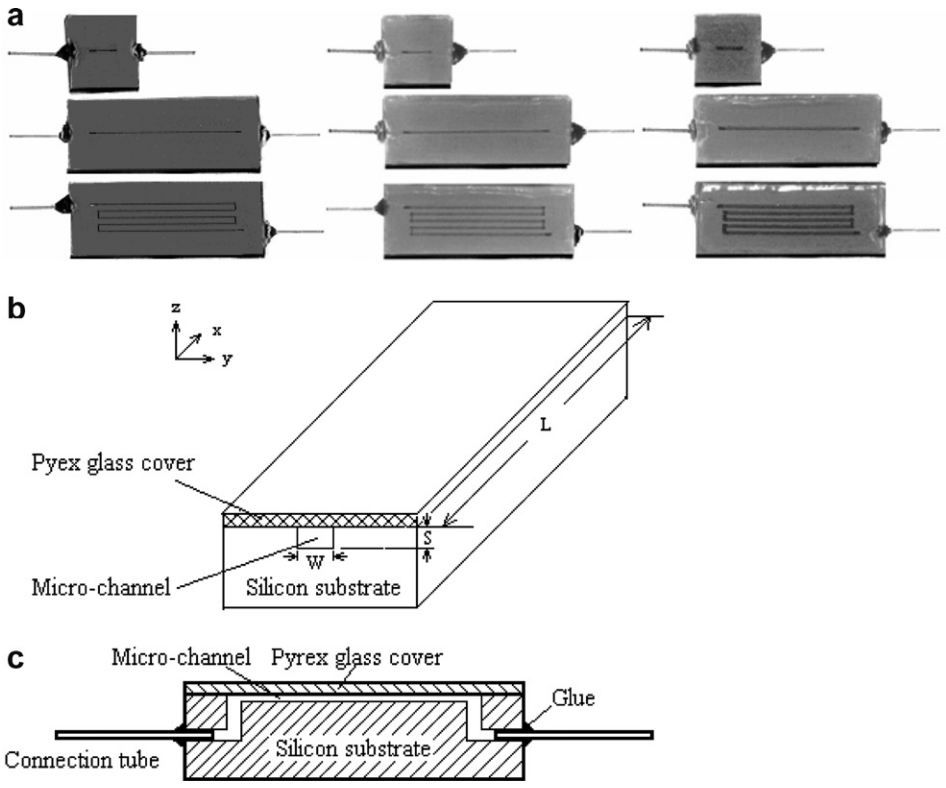

Fig. 1. (a) Photograph of three groups of micro-channels; (b) schematic of the straight micro-channel; (c) schematic of inlet and outlet elbows.

Table 1
Dimensions of three groups of micro-channels

Channel group No.	Width $W \pm 2$ μm	Depth $S \pm 2$ μm	Hydraulic diameter D_h (mm)	Total length of the micro-channels $L \pm 0.3$ mm		
				Long channel L_l (mm)	Short channel L_{sh} (mm)	Serpentine channel L_s (mm)
Channel 1	213	206	0.2094	23.6	4.1	118
Channel 2	419	406	0.4124	23.5	4	117.5
Channel 3	630	615	0.6224	23.8	4.2	119

Instrument), a 60 ml syringe (Mcmaster), a micro-filter (Swagelok), pressure transducers (Kavlico), micro-channel test sections and computerized data acquisition system.

To measure the pressure drop, the water at flow rates ranging from 0.1 ml/min to 70 ml/min, which can be set on the panel of the infusion pump with an accuracy of ±0.5%, was driven to the micro-channel test section. The 2 μm micro-filter can remove any particles or bubbles which may block the micro-channel before the flow enters into the test section. Two pressure transducers with a ±0.5% FS accuracy were installed at the inlet and outlet of the micro-channel, respectively to measure the upstream and downstream pressure and then logged through a data acquisition system. To measure the upstream pressure accurately, two pressure transducers with different measurement ranges were used. The one with a large measurement range (0–100PSI) was used for smaller micro-channels/larger flow rates, and the other one with a small range (0–15PSI) were used for larger micro-channels/smaller flow rates. The data acquisition system started recording when the flow can be considered as steady state. The test sections were placed horizontally, and all experiments were conducted in room temperature.

Due to the relatively short length of the micro-channels used in this work, the inlet and outlet pressure losses can not be neglected. These pressure losses were estimated by some empirical formulations in many previous studies, which may not be accurate enough. To achieve the measurement of accurate frictional pressure drops, two straight micro-channels with the same channel size but different channel lengths were fabricated. The inlet and outlet losses are the same for both long and short channels because of the same structure and flow conditions. Hence, the difference between the pressure drop of the long straight micro-channel and that of the short straight micro-channel is therefore the pressure drop without inlet and outlet losses.

After measuring the pressure drop in micro-channels, the flow structure around the corner of the serpentine

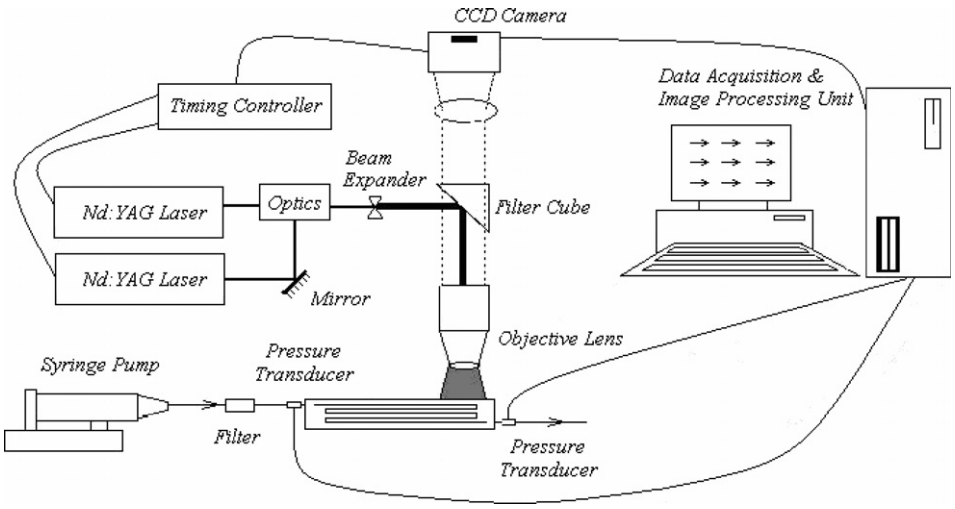

Fig. 2. Schematic of the experimental apparatus (water used for pressure drop experiment and water + fluorescent particles for micro-PIV experiment).

micro-channel need to be visualized. A micro-particle image velocimetry (micro-PIV) was used where fluorescent particles (Duke Scientific) were seeded into the de-ionized water flow. Two Nd:YAG lasers were directed to the same optical path by optical lenses and expanded by a beam expander made up of a concave and a convex lens. The 0.69 μm particles absorb green light (~542 nm) and emit red light (~612 nm). The emitted light is imaged through a 10× objectives lens (NA = 0.3) and passed to the fluorescent filter cube, where the green light from background reflection is filtered out and the red fluorescence from the sub-micron particles is passed to the 0.5× lens and recorded on the CCD camera. To achieve this spatial resolution required a volumetric particle concentration of approximately 0.0082%. This volume fraction of seed particles is small enough to neglect any two-phase effects, and the working fluid can be considered a single-phase fluid. In this work, this time delay is set to be 1–15 μs for the micro-channel flow at different Re numbers, so the particles move approximately 1/4th of an interrogation window between pulses. The interrogation windows measure 32 camera pixels square, thus the particles moves approximately 8 pixels between laser pulses. Assume that the measured velocity is accurate to within 1/5th of a pixel. It results in an experimental uncertainty of less than ±2.5% [30].

3. Data reduction and analysis

For a fully developed laminar flow in a rectangular channel with an aspect ratio α, Shah and London [31] used a power series for the friction factor and fitted the coefficients using their experimental data as below:

$$(fRe)_{\mathrm{fd}} = 96(1 - 1.3553\alpha + 1.9467\alpha^2 - 1.7012\alpha^3 + 0.9564\alpha^4 - 0.2537\alpha^5) \quad (1)$$

This empirical equation can approximate the two-dimensional theoretical exact solution [32] for the fully developed friction factor with an error less than 0.05%. Then the frictional pressure drop in a channel with fully developed flow can be written as

$$\Delta P_{\mathrm{fd}} = \frac{(fRe)_{\mathrm{fd}} \Delta L \mu Q}{2 D_{\mathrm{h}}^2 A} \quad (2)$$

However, the current micro-channels may not be long enough for the flow to become fully developed under laminar flow conditions. The flow conditions need to be verified.

For a laminar flow in a rectangular channel, the length of the developing flow in the entrance region can be estimated by the following equation given by Shah and London [31]:

$$L_{\mathrm{d}} = (0.06 + 0.07\alpha - 0.04\alpha^2) Re D_{\mathrm{h}} \quad (3)$$

Table 2 shows the minimum and maximum $L_{\mathrm{d}}/D_{\mathrm{h}}$ for the flow rate range in our experiment and the L/D_{h} for the current short and long channels. It is clear that for a substantial number of cases, the flows may not be fully developed under the current experimental conditions.

For a developing flow, the pressure drop from the inlet of the channel to a downstream location x in the entrance region is the sum of the fully developed pressure drop and the pressure drop defect given by the equation below [33]:

$$\Delta P_{\mathrm{dev}} = [(fRe)_{\mathrm{fd}} x^+ + K(x^+)] \frac{\rho U^2}{2} \quad (4)$$

$$x^+ = \frac{x}{Re \cdot D_{\mathrm{h}}} \quad (5)$$

where $K(x^+)$ is the pressure drop defect given by

$$K(x^+) = [f_{\mathrm{app}} Re - (fRe)_{\mathrm{fd}}] x^+ \quad (6)$$

$$f_{\mathrm{app}} Re = 4 \left\{ \frac{3.44}{(x^+)^{0.5}} + \frac{K(\infty)/(4x^+) + (fRe)_{\mathrm{fd}}/4 - 3.44/(x^+)^{0.5}}{1 + B(x^+)^{-2}} \right\} \quad (7)$$

where f_{app} is the apparent friction factor and Eq. (7) is given in Kakac et al. [33]. According to White [34], the

Table 2
Comparison of current pipe lengths with those of entrance regions

Re	L_d/D_h	L/D_h (straight short one)			L/D_h (straight long one)		
		Channel 1	Channel 2	Channel 3	Channel 1	Channel 2	Channel 3
Minimum: 47	4.23						
Maximum: 2268	204.12	19.58	9.70	6.74	112.7	56.98	38.24

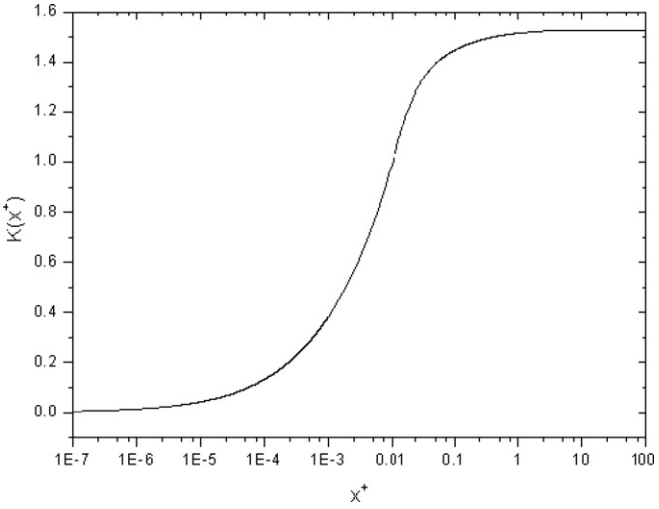

Fig. 3. Pressure drop defect $K(x^+)$ vs. x^+.

constant B in Eq. (7) is equal to 2.93×10^{-4}. As plotted in Fig. 3, the pressure drop defect $K(x^+)$ for the current micro-channels begins at the value of 0 for $x^+ = 0$ and increases asymptotically to the fully developed constant value $K(\infty)$ which has a dependence upon the channel aspect ratio for rectangular channels as suggested by Shah and London [31]:

$$K(\infty) = 0.6796 + 1.2197\alpha + 3.3089\alpha^2 - 9.5921\alpha^3 + 8.9089\alpha^4 - 2.9959\alpha^5 \quad (8)$$

Eq. (8) determines the fully developed $K(\infty)$ for a rectangular channel with an uncertainty of 0.04%.

The pressure drop for the straight short, ΔP_{sh}, and straight long channel, ΔP_l, can be expressed as

$$\Delta P_{sh} = \Delta P_{io} + \Delta P_{dev}(x = L_{sh}) \quad (9)$$

$$\Delta P_l = \Delta P_{io} + \Delta P_{dev}(x = L_l) \quad (10)$$

where ΔP_{io} is the inlet and outlet assembly losses due to changes in tubing diameter, tees and elbows as indicated in Fig. 1(c). ΔP_{io} is same for both long and short channels because of the same structure and flow conditions. ΔP_{sh} and ΔP_l are the measured pressure drops for the straight short and straight long channels, respectively. Combine Eqs. (4)–(10), the experimental friction factor that takes the entrance effect into consideration is estimated by the following equation:

$$f_{exp} = \left\{ \frac{\Delta P_l - \Delta P_{sh}}{\rho U^2/2} - [K(L_l) - K(L_{sh})] \right\} \frac{D_h}{L_l - L_{sh}} \quad (11)$$

For the serpentine micro-channels, the measure pressure drop can be expressed as

$$\Delta P_s = \Delta P_{io} + \Delta P_{dev}(x = L_s) + N \cdot \Delta P_b \quad (12)$$

where ΔP_s is the measured pressure drop for the serpentine channel and ΔP_b is the additional pressure drop due to the miter bend. N is the number of miter bends. So ΔP_b and the bend loss coefficient, K_b, can be written as

$$\Delta P_b = \frac{\frac{\Delta P_s - \Delta P_l}{\rho U^2/2} - \left[\left\{ \frac{\Delta P_l - \Delta P_{sh}}{\rho U^2/2} - [K(L_l) - K(L_{sh})] \right\} \frac{L_s - L_l}{L_l - L_{sh}} + K(L_s) - K(L_l) \right]}{N / \frac{\rho U^2}{2}} \quad (13)$$

$$K_b = \frac{\Delta P_b A^2}{2\rho Q^2} = \frac{\frac{\Delta P_s - \Delta P_l}{\rho U^2/2} - \left[\left\{ \frac{\Delta P_l - \Delta P_{sh}}{\rho U^2/2} - [K(L_l) - K(L_{sh})] \right\} \frac{L_s - L_l}{L_l - L_{sh}} + K(L_s) - K(L_l) \right]}{N} \quad (14)$$

According to the error propagation analysis, the uncertainty range of the bend loss coefficient can be calculated to be ±12.3% to ±16.1%.

4. Micro-PIV system validation

To validate the micro-PIV system, the velocity field is initially obtained at room temperature in the channel 1 at low Re numbers. The time delay between consecutive frames is 5 ms. An interrogation window of 32×32 pixels and a grid size of 16×16 pixels are used. The analytical solution for the velocity profile at the PIV measurement depth can be formulated as

$$u(y) = -\frac{W^2}{2\mu}\frac{dP}{dx}\left[\frac{y}{W} - \frac{y^2}{W^2}\left(\frac{2}{\pi}\right)^3 \times \sum_{k=0}^{\infty}\frac{(-1)^k}{(2k+1)^3}\frac{\cosh\left[(2k+1)\frac{\pi z_m}{2W}\right]}{\cosh\left[(2k+1)\frac{\pi S}{2W}\right]} \times \cos\left[(2k+1)\frac{\pi(2y-W)}{2W}\right]\right] \quad (15)$$

where dP/dx is the pressure gradient, W and S are the width and depth of the micro-channel, respectively. The depth of field z_m is described by Meinhart et al. [35] as

$$z_m = \frac{3n\lambda}{NA^2} + \frac{2.16D_p}{\tan\theta} + D_p \quad (16)$$

where n is the index of refraction of the immersion medium between the micro-fluidic device and the objective lens, λ is the wavelength of light in a vacuum, NA is the numerical aperture of the objective lens, D_p is the diameter of the PIV particle and θ is the small light collection angle. In our case, n was 1, λ was 612 nm, NA was 0.3, d was 0.69 μm and $\tan\theta$ was 0.31. Therefore, the depth of field was calculated to be 26.06 μm. Fig. 4 shows the measurements of micro-PIV in the micro-channel of 0.209 mm and comparison with the theoretical profile computed from Eq. (15).

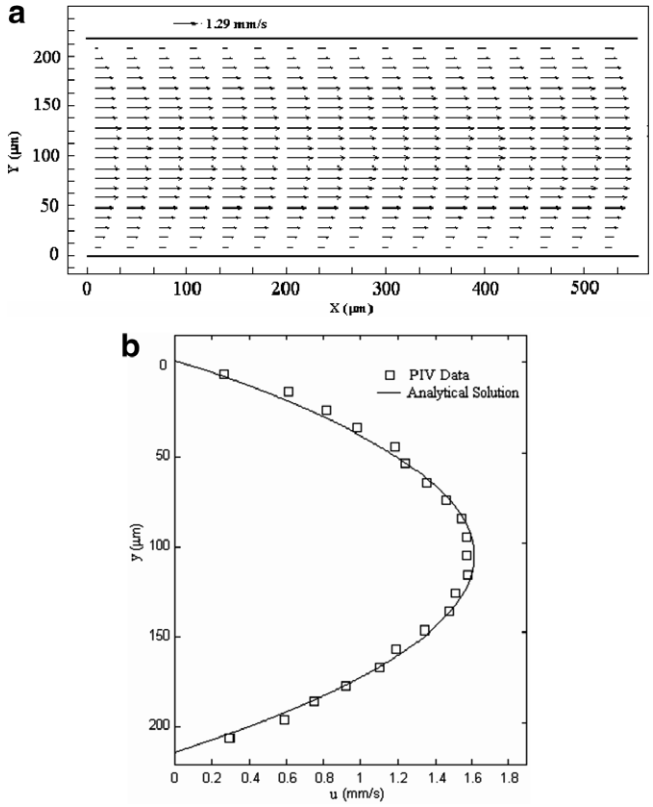

Fig. 4. Micro-PIV results for low speed flow. (a) Velocity vectors (113 pairs of images were ensemble-averaged). (b) Comparison with the theoretical profile ($Re = 0.3$).

5. Experimental results

5.1. Flow structures around the miter bend

Fig. 5 shows typical velocity vectors field generated by the micro-PIV system. The focus of the flow field in Fig. 5 is the effects of the 90° turning on the flow micro-structures around the miter bend in the serpentine micro-channel at $Re = 500$. We note that the main stream velocity increases while the flow is rounding the corner. It is also apparent that micro-structures of flow recirculation have formed around the outer corner and immediately after the inner corner (flow separation). A detailed visualization and discussion on the onset and development of induced vortices around the outer and inner corners with the Re number are given below. Fig. 6(a)–(e) shows the enlarged velocity fields at the outer corner for the Reynolds numbers ranging from 100 to 1500. Fig. 6(f)–(j) shows the enlarged velocity fields at the inner corner for the same Reynolds numbers. Fig. 7 shows the corresponding streamlines computed from the experimental velocity vectors. For the induced micro-flow structures at the outer corner, there is basically no recirculation for $Re = 100$ and only some fluctuations in the flow adjacent to the wall due to the wall roughness are captured by the PIV. At $Re = 300$, a very small vortex located at ($x = 0.2$ mm, $y = 0.95$ mm) is seen, but its circulatory motion is not fully developed. It is clear that at $Re = 500$, the recirculation vortex is fully developed and located at ($x = 0.3$ mm, $y = 1.07$ mm). As the Reynolds number is further increased to 1000 (Fig. 6(d)) and then to 1500 (Fig. 6(e)), the locations of recirculation vortices stay at the same point and only the size and strength are increased with the Reynolds number.

For flow structures near the inner corner, the micro-flow structures that form due the flow separation always start right after the sharp edge as the flow separates. Again, there is basically no separation vortex for $Re = 100$. The separation vortex is very clear for $Re = 300$. As the

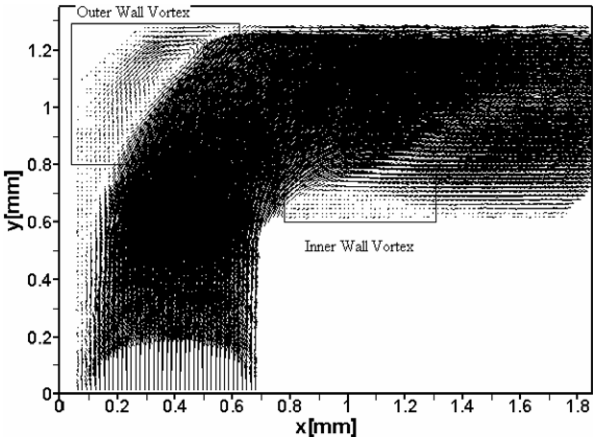

Fig. 5. Typical velocity vectors in the serpentine micro-channel at $Re = 500$.

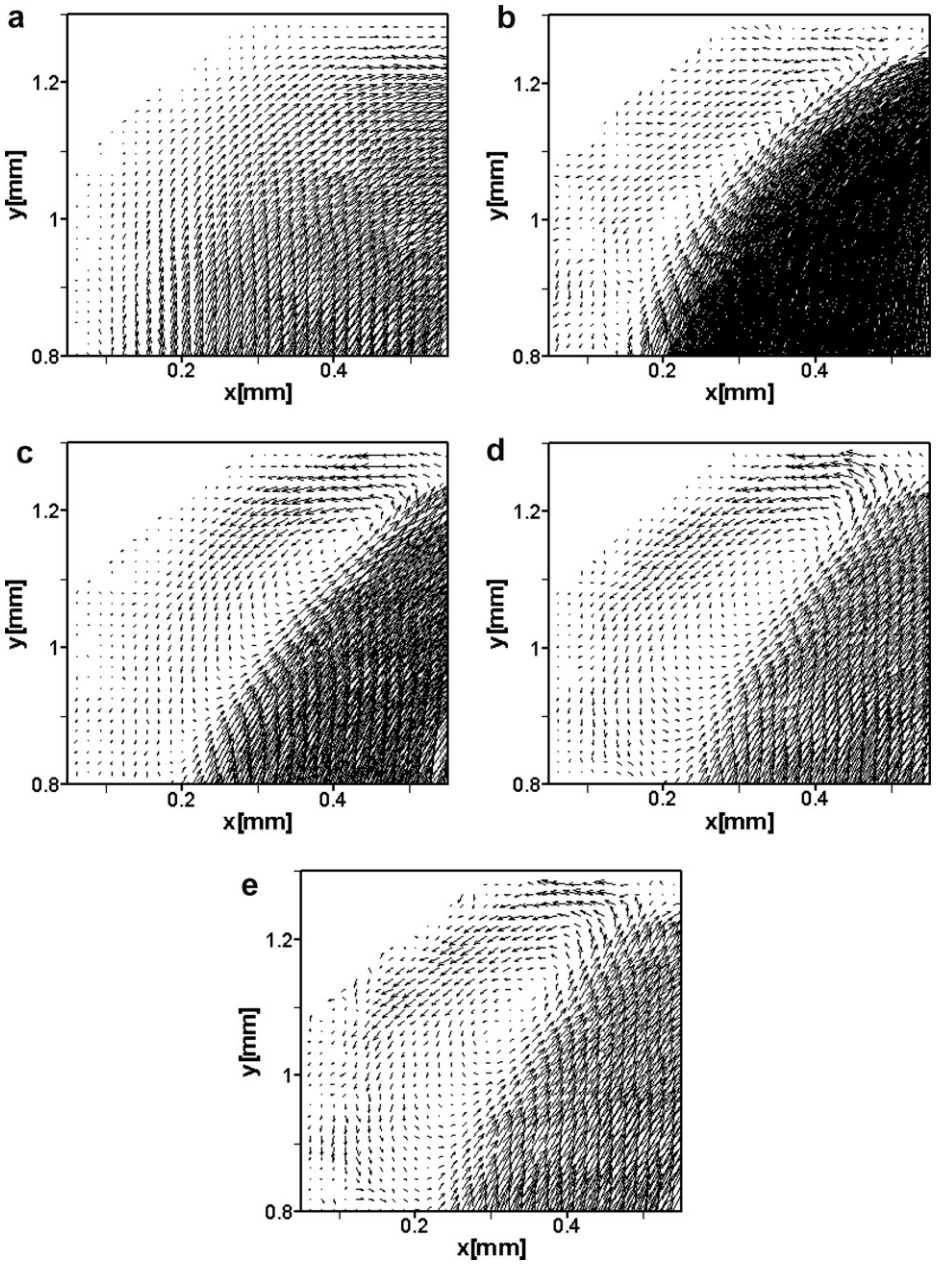

Fig. 6. Flow structure at the outer wall for (a) $Re = 100$; (b) $Re = 300$; (c) $Re = 500$; (d) $Re = 1000$; (e) $Re = 1500$ and at the inner wall for (f) $Re = 100$; (g) $Re = 300$; (h) $Re = 500$; (i) $Re = 1000$; (j) $Re = 1500$.

Reynolds number is further increased, the size and strength of the separation vortex are also increased accordingly. However, the growth of the vortex seems saturated after $Re = 1000$ as there is no significant difference in the size between $Re = 1000$ and $Re = 1500$ but the strength continues to increase as discussed later. For $Re = 1000$, the inner corner vortex approximately occupies 20% of the width of the channel in the downstream of the bend.

5.2. Pressure drop

Fig. 8 shows the measured bend pressure drops due to the 90° turn in the serpentine micro-channel as a function of the Reynolds number for three different channel sizes. When $Re < 100$, the bend pressure drops are very small and negligible for all of the channels. While as $Re > 100$, the bend pressure drops increase exponentially with the Reynolds number. This result is consistent with the findings of the above experimental visualization of flow structures. When $Re < 100$, there is no flow separation and recirculation. The way the flow passes the bend is similar to that for the flow passing through the straight channel, so the bend additional pressure drop is very small. When $Re > 100$, the recirculation appears and develops along the channel, so the pressure drop due to the bend increases. From Fig. 8, the additional pressure drop due to bending

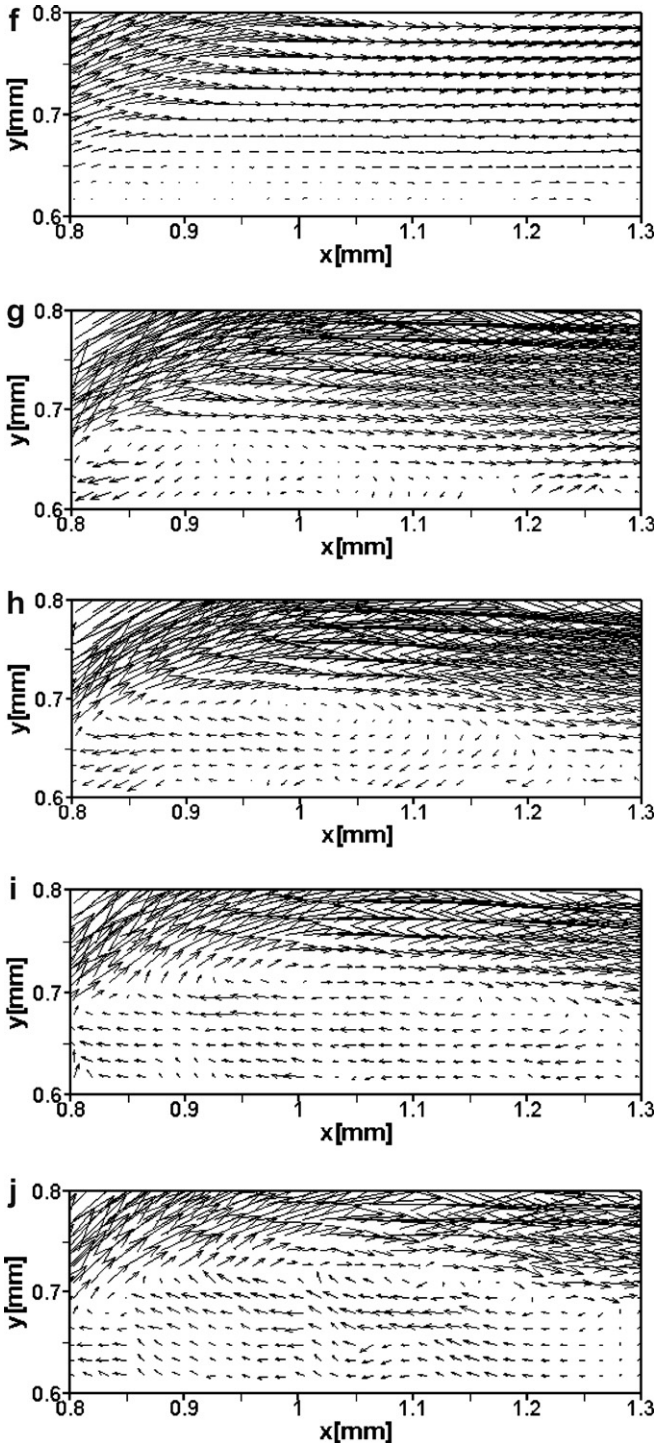

Fig. 6 (*continued*)

of the micro-channel with hydraulic diameter 0.209 mm is around 53 kPa when the *Re* number reaches around 850, which is approximately equal to the frictional pressure drop of the same size straight micro-channel with 23.7 mm length, 101% of the current total length. Hence, the additional pressure drop due to the miter bend is also a substantial source of the micro-channel pressure drop, especially for small size and short length micro-channels.

In order to further substantiate the relatively large bend pressure drops, we calculated the circulation, Γ, for every induced vortex from the velocity field given in Fig. 6. The circulation, Γ, that is the strength of the vortex is defined as

$$\Gamma = \int\int (\nabla \times \vec{V}) \cdot \mathrm{d}\vec{A} \tag{17}$$

The results of the calculated vortex circulation are given in Table 3. In general, the outer vortices are three to six times stronger than the inner vortices. Fig. 9 shows the total vortex circulations as a function of the Reynolds number. The total circulation is the sum of the absolute values of the inner and outer vortices. The similar trends between the total vortex circulation (Fig. 9) and the bend pressure drop (Fig. 8) serve to confirm the measured data.

Since the maximum *Re* number produced by our pump was only around 850 for channel 1, therefore, the bend loss coefficient range is limited. Here the bend loss coefficients for all three channels are evaluated by using Eq. (14) and shown in Fig. 10. The horizontal solid line represents the miter bend loss coefficient of 1.1 which is reported by Streeter [36] for macro-scale turbulent flow applications. From Fig. 10, we can see that bend loss coefficients of the micro-channels are all larger than 1.1. It is a similar conclusion to that of Yamashita et al. [10], who also reported the bend loss coefficient in the laminar flow region is larger than that in the turbulent region. It decreases with increasing *Re* number, which is also different from the trend in the turbulent flow. For a macro-channel turbulent flow at a larger *Re* number, K_b almost does not change with the *Re* number. When the *Re* is larger than some value between 1300 and 1500, K_b almost keeps constant and changes in the range of $\pm 10\%$. A size effect on K_b is also observed. It is larger for smaller channel when there is flow separation, namely $Re > 100$–200. After considering the measurement uncertainty, these three curves still have some differences.

6. Summary

The investigation of a pressure-driven water flow in serpentine micro-channels with miter bends was conducted experimentally. The micro-channels have rectangular cross-sections with hydraulic diameters of 0.209 mm, 0.412 mm and 0.622 mm, respectively. The main objective is to research on the bend effect on the pressure drop and flow structure in micro-scale, other parameters are not considered such as surface roughness, wettability, etc. The following conclusions were obtained:

(1) The flow micro-structures around the bend of a serpentine micro-channel can be divided into three categories depending on the flow Reynolds number. When $Re < 100$, there is no induced flow recirculation and flow separation. When $Re > 100$, vortices and flow separation appear and further develop. The outer corner vortex develops along the wall of the channel, and the vortex center moves slightly from the upper stream to

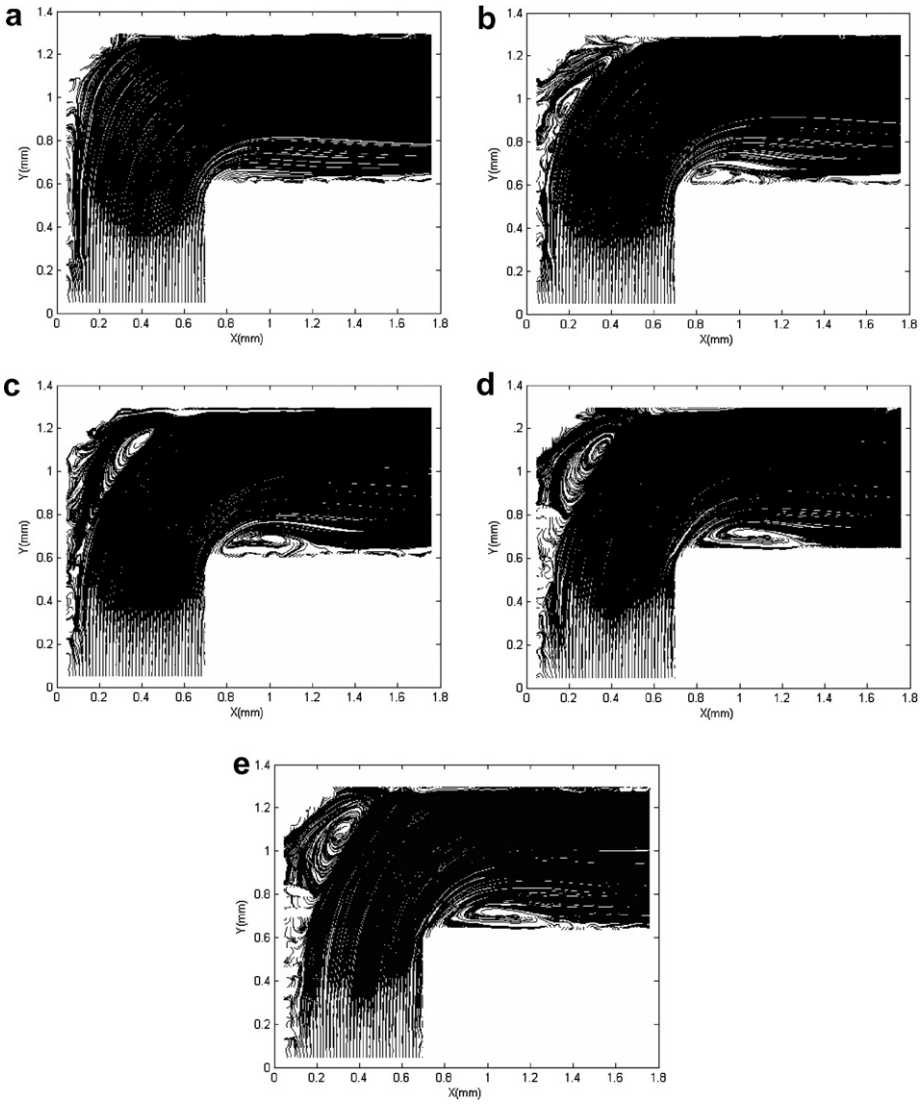

Fig. 7. Streamline for (a) $Re = 100$, (b) $Re = 300$, (c) $Re = 500$, (d) $Re = 1000$, and (e) $Re = 1500$.

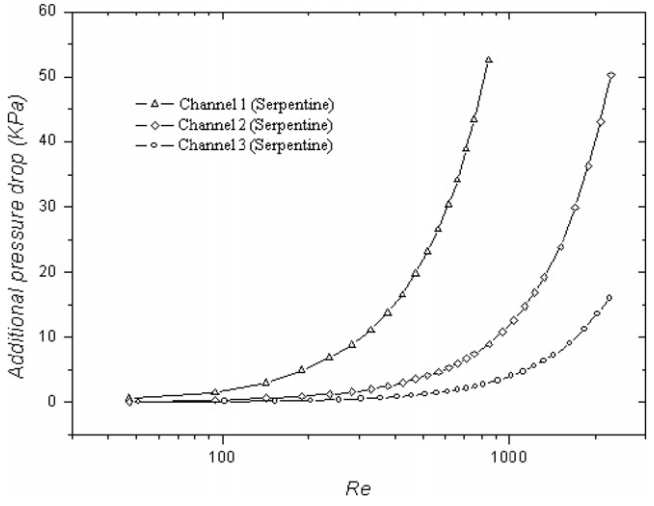

Fig. 8. Bend additional pressure drops vs. *Re* number in serpentine microchannels.

the down stream with the increasing of the *Re* number. The inner wall vortex due to flow separation develops immediately after the flow makes the turn. When *Re* is around 1000, the inner wall vortex approximately occupies 20% of the width of the channel in the downstream side of the bend. When $Re > 1000$–1500, the shape and size of the outer and inner vortices become almost constant.

Table 3
Calculated vortex circulation

Re	Inner wall vortex strength (mm^2/s)	Outer wall vortex strength (mm^2/s)
100	0.082	−0.41
300	4.10	−12.47
500	10.97	−77.48
1000	28.10	−203.9
1500	97.99	−266.9

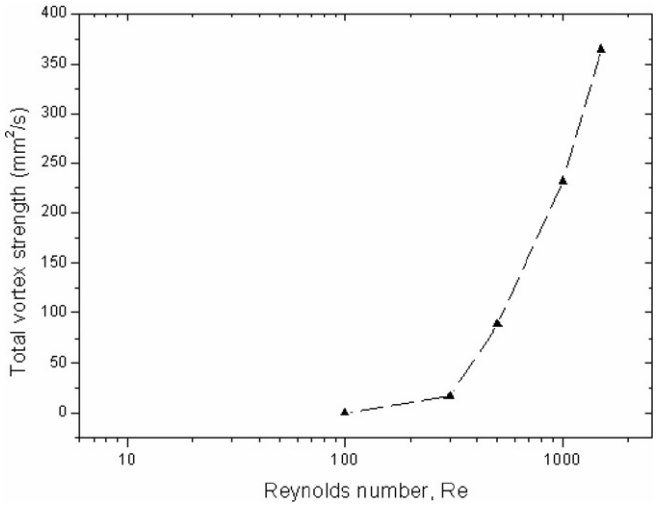

Fig. 9. Total vortex circulation vs. Reynolds number.

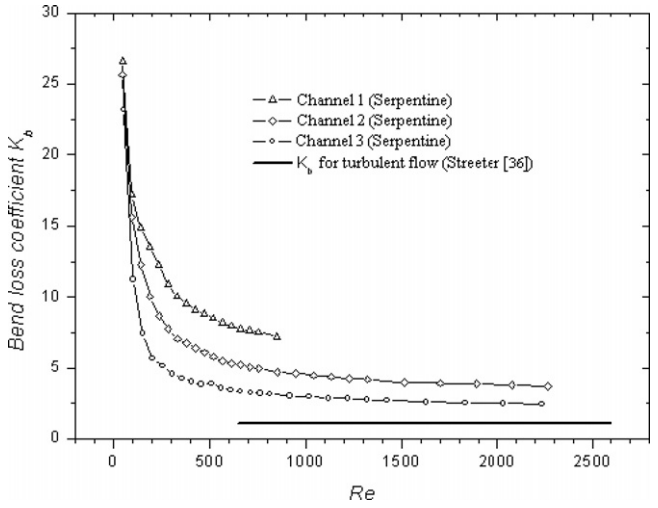

Fig. 10. Bend loss coefficients vs. *Re* number in serpentine micro-channels.

(2) In serpentine micro-channels, the additional pressure drop due to miter bends can be divided into two groups. The first group is for $Re < 100$ where there is no eddies and the additional pressure drop is very small for all of the channels. The other group is for flows with the Reynolds numbers exceeding the threshold value that is in the range of 100–300. When the Reynolds is higher than the threshold value, we found the flow separation and formation of vortices that appear on the inner and outer wall around the miter bend. These vortices increase in strength with increasing *Re* number that causes the bend pressure drop to increase sharply with the *Re* number. The experimental results also show the bend pressure drop increases with decreasing hydraulic diameters. Bend loss coefficient K_b is a function of the *Re* number only when $Re < 100$, a function of the *Re* number and channel size when $Re > 100$, and almost keeps constant and changes in the range of $\pm 10\%$ when *Re* is larger than some value in 1000–1500. A major finding is that the K_b is different from the value 1.1 used for the macro-channels in engineering applications. The trend of the experimental pressure drop is consistent with the flow structure change.

Acknowledgements

This research was supported by the NASA Hydrogen Research for Spaceport and Space Based Applications at the University of Florida (Grant number NAG3-2930). The partial support by the Andrew H. Hines, Jr./Progress Energy Endowment Fund is also acknowledged.

References

[1] C.M. Ho, Y.C. Tai, Micro-electro-mechanical-systems (MEMS) and fluid flows, Annu. Rev. Fluid Mech. 30 (1998) 579–612.
[2] C. Hong, Y. Asako, Heat transfer characteristics of gaseous flows in a microchannel and a microtube with constant wall temperature, Numer. Heat Transfer A 52 (2007) 219–238.
[3] C.E. Zhen, Z.C. Hong, Y.J. Lin, N.T. Hong, Comparison of 3D and 2D DSMC heat transfer calculations of low-speed short microchannel flows, Numer. Heat Transfer A 52 (2007) 239–250.
[4] P.S. Glockner, G.F. Naterer, Numerical simulation of electrokinetic flow and heat transfer in microchannels with a finite-volume method, Numer. Heat Transfer A 49 (2006) 451–470.
[5] S.L. Broderick, B.W. Webb, D. Maynes, Thermally developing electro-osmotic convection in microchannels with finite Debye-layer thickness, Numer. Heat Transfer A 48 (2005) 941–964.
[6] O.M. Haddad, M.M. Abuzaid, M.A. Alnumr, Developing free-convection gas flow in a vertical open-ended microchannel filled with porous media, Numer. Heat Transfer A 48 (2005) 693–710.
[7] S.A. Berger, L. Talbot, L.S. Yao, Flow in curved pipes, Annu. Rev. Fluid Mech. 15 (1983) 461–512.
[8] P. Hille, R. Vehrenkamp, E.O. Schulzdubois, The development and structure of primary and secondary flow in a curved square duct, J. Fluid Mech. 151 (1985) 219–241.
[9] G. Heskestad, Two-dimensional miter-bend flow, J. Basic Eng. 93 (1971) 433–437.
[10] H. Yamashita, R. Izumi, G. Kushida, T. Mizuno, Fluid flow and heat transfer in a two-dimensional miter-bend (1st report, experiments and analysis), Bull. JSME 29 (1986) 4164–4169.
[11] J.M. Choi, N.K. Anand, Heat transfer in a serpentine channel with a series of right-angle turns, Numer. Heat Transfer A 23 (1993) 189–210.
[12] S. Chintada, K.H. Ko, N.K. Anand, Heat transfer in 3D serpentine channels with right-angle turns, Numer. Heat Transfer A 36 (1999) 781–806.
[13] S. Etemad, B. Sunden, Numerical investigation of turbulent heat transfer in a rectangular-sectioned 90° bend, Numer. Heat Transfer A 49 (2006) 323–343.
[14] S.Y.K. Lee, M. Wong, Y. Zohar, Gas flow in microchannels with bends, J. Micromech. Microeng. 11 (2001) 635–644.
[15] S. Maharudrayya, S. Jayanti, A.P. Deshpande, Pressure losses in laminar flow through serpentine channels in fuel cell stacks, J. Power Sources 138 (2004) 1–13.
[16] P. Wu, W.A. Little, Measurement of friction factors for the flow of gases in very fine channels used for microminiature Joule–Thomson refrigerators, Cryogenics 23 (1983) 273–277.
[17] X.F. Peng, G.P. Peterson, Convective heat transfer and flow friction for water flow in microchannel structures, Int. J. Heat Mass Transfer 39 (1996) 2599–2608.

[18] G.M. Mala, D. Li, Flow characteristics of water in microtubes, Int. J. Heat Fluid Flow 20 (1999) 142–148.
[19] W.L. Qu, G.M. Mala, D. Li, Pressure-driven water flows in trapezoidal silicon microchannels, Int. J. Heat Mass Transfer 43 (2000) 353–364.
[20] Z.X. Li, D.X. Du, Z.Y. Guo, Experimental study on flow characteristics of liquid in circular micro-tubes, Microscale Thermophys. Eng. 7 (2003) 253–265.
[21] J. Judy, D. Maynes, B.W. Webb, Characterization of frictional pressure drop for liquid flows through microchannels, Int. J. Heat Mass Transfer 45 (2002) 3477–3489.
[22] H.Y. Wu, P. Cheng, Friction factors in smooth trapezoidal silicon microchannels with different aspect ratios, Int. J. Heat Mass Transfer 46 (2003) 2519–2525.
[23] G. Hetsroni, A. Mostak, E. Pogrebnyak, L.P. Yarin, Fluid flow in micro-channels, Int. J. Heat Mass Transfer 48 (2005) 1982–1998.
[24] M.J. Kohl, S.I. Abdel-Khalik, S.M. Jeter, D.L. Sadowski, An experimental investigation of microchannel flow with internal pressure measurements, Int. J. Heat Mass Transfer 48 (2005) 1518–1533.
[25] Y.W. Hwang, M.S. Kim, The pressure drop in microtubes and the correlation development, Int. J. Heat Mass Transfer 49 (2006) 1804–1812.
[26] S.T. Tan, E.Y.K. Ng, Numerical analysis of EDL effect on heat transfer characteristic of 3D developing flow in a microchannel, Numer. Heat Transfer A 49 (2006) 991–1007.
[27] J.M. Koo, C. Kleinstreuer, Liquid flow in microchannels: experimental observations and computational analyses of microfluidics effects, J. Micromech. Microeng. 13 (2003) 568–579.
[28] T. Bayraktar, S.B. Pidugu, Characterization of liquid flows in microfluidic systems, Int. J. Heat Mass Transfer 49 (2006) 815–824.
[29] I. Hassan, Thermal-fluid MEMS devices: a decade of progress and challenges ahead, J. Heat Transfer 128 (2006) 1221–1233.
[30] A.K. Prasad, R.J. Adrian, C.C. Landreth, P.W. Offutt, Effect of resolution on the speed and accuracy of particle image velocimetry interrogation, Exp. Fluids 13 (1992) 105–116.
[31] R.K. Shah, A.L. London, Laminar flow forced convection in ducts, Advances in Heat Transfer, Supplement 1, Academic Press, New York, 1978.
[32] N. Nguyen, S.T. Wereley, Fundamentals and Applications of Microfluidics, second ed., Artech House, Boston, 2006.
[33] S. Kakac, R.K. Shah, W. Aung, Handbook of Single-Phase Convective Heat Transfer, John Wiley and Sons, New York, 1987.
[34] F.M. White, Viscous Fluid Flow, second ed., McGraw-Hill, New York, 1991.
[35] C.D. Meinhart, S.T. Wereley, M.H.B. Gray, Volume illumination for two-dimensional particle image velocimetry, Meas. Sci. Technol. 11 (2000) 809–814.
[36] V.L. Streeter, Handbook of Fluid Dynamics, McGraw-Hill, New York, 1961.